

## 5

# Characteristics of planetary systems

DEBRA FISCHER AND JI WANG

Philosophical musings that other worlds might exist date back more than 2000 years to the ancient Greeks. We live in a fortunate time, when the discovery of exoplanets has the potential to address questions about how planetary systems form and evolve. In what ways do exoplanetary systems mirror our solar system? How are they different? Does the presence of a binary star affect planet formation? Are Earth analogs common? Does the energy from other stars give rise to life?

Confirmed and candidate exoplanets number in the thousands and search techniques include Doppler measurements, transit photometry, microlensing, direct imaging, and astrometry. Each detection technique has some type of observational incompleteness that imposes a biased view of the underlying population of exoplanets. In some cases, statistical corrections can be applied. For example, transiting planets can only be observed if the orbital inclination is smaller than a few degrees from an edge-on configuration. However, with the reasonable assumption of randomly oriented orbits, a geometrical correction can be applied to determine the occurrence rate for all orbital inclinations. In other cases, there is simply no information about the underlying population and it is not possible to apply a meaningful correction. For example, the number of planets with a similar mass (or radius) and a similar intensity of intercepted stellar flux as our Earth is not secure at this time because the number of confirmed detections for this type of planet is vanishingly small.

As a result of the sample biases and observational incompleteness for each discovery technique, our view of exoplanet architectures is fuzzy at best. There are no cases beyond the solar system where the entire parameter space for orbiting planets has been observed. Instead, we piece together an understanding of exoplanet architectures by counting planets in the regimes where techniques are robust and then we estimate correction factors when possible. When drawing conclusions about the statistics of exoplanets, it is helpful to understand completeness in this underlying patchwork of orbital parameter space.

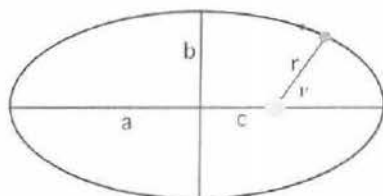


Fig. 5.1 Geometry of an elliptical orbit with semi-major axis  $a$ , semi-minor axis  $b$ , and eccentricity  $e = c/a$ .

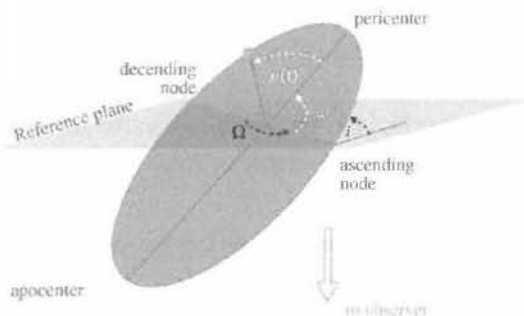


Fig. 5.2 Orbital angles  $i$ ,  $\omega$ , and  $\Omega$  define the orientation of the orbit with respect to the plane of the sky.

We begin by reviewing the exoplanet detection techniques with particular consideration of the observational biases and then discuss the implications for planet formation with an eye toward how our solar system compares.

## 5.1 Overview of Keplerian orbits

The motion of planets around the Sun was famously deciphered by Johannes Kepler. Kepler's first law states that planets orbit in an ellipse with the star at the focus; the second law is a statement about conservation of angular momentum – planets sweep out equal areas in equal time intervals; the third law says that the square of the orbital period is proportional to the cube of the semi-major axis. Kepler's laws were later generalized by Isaac Newton in his universal law of gravitation.

The fundamental plane of an elliptical orbit is shown in Fig. 5.1 with the star at the focus of the ellipse. The ellipse is parametrized by the semi-major axis  $a$ , and the semi-minor axis  $b$ . The orbital eccentricity is defined as the ratio of  $c/a$ , and the planet sweeps out an angle  $\nu$ , which is referenced to the point of periastron.

In practice, the orbital plane is randomly oriented in space. Figure 5.2 shows the angles that define the orientation of the fundamental elliptical orbit with respect to

the plane of the sky. First, imagine that the plane of the sky (the reference plane) passes through the star-centered focus of the ellipse; the intersection of these two planes is called the line of nodes. The orientation of periastron passage is defined by  $\omega$ ;  $\omega = 90^\circ$  or  $270^\circ$  if we are looking along the long semi-major axis of the orbit. The inclination,  $i$ , references the tilt of the orbit and is defined so that  $i = 90^\circ$  when the orbit is viewed edge-on and  $i = 0^\circ$  when viewed face-on. For the special case of a circular orbit,  $e = 0$  and there is no periastron point, so  $\omega$  is undefined for circular orbits. The third angle,  $\Omega$ , is a rotation perpendicular to the plane of the sky. This last angle is not relevant for Doppler observations (because it does not change the radial component of the velocity) or for transit observations; it can only be measured with direct imaging or astrometric techniques.

Although the planetary orbits have been shown in the reference frame of the star, the star and planet actually orbit the center of mass (COM).

## 5.2 Doppler surveys for exoplanets

Doppler surveys have detected more than 500 planets and this was the first successful technique for detecting planets outside our solar system. This technique is unique in providing masses for exoplanets, modulo the generally unknown orbital inclination. The first detected planets were gas giants that orbit close to their host stars. This turned out to be a bias of this technique: close-in gas giants exert the largest possible gravitational force on the host star and produce the most significant stellar reflex velocities. While improvements in this technique have permitted the detection of one planet with a mass similar to the Earth, this technique has severe incompleteness with decreasing mass and increasing orbital periods.

### 5.2.1 The Doppler effect

Owing to the Doppler effect, spectral lines from the stellar atmosphere are periodically blue-shifted and then red-shifted as the star orbits the COM over one orbital period. Only the velocity component along the line of sight (the radial velocity) between the observer and the source produces a Doppler shift.

An emitted photon of wavelength  $\lambda_0$  will be Doppler shifted to a new wavelength  $\lambda$  as described by the theory of special relativity (Einstein, 1905). The reflex velocities that planets induce in their host stars are typically small. For example, the reflex solar velocity from Jupiter is  $\sim 12 \text{ m s}^{-1}$  and the tug of the Earth on the Sun is a mere  $0.1 \text{ m s}^{-1}$ . The Doppler shift can safely be expressed in the non-relativistic form without incurring any measurable errors:

$$\lambda = \lambda_0 \left( 1 + \frac{v}{c} \right). \quad (5.1)$$

When calculating the velocity of a source star, the velocity of the observer (the “barycentric velocity”) must be subtracted from the measured radial velocity in order to recover the velocity of the source. The Jet Propulsion Lab’s HORIZONS<sup>1</sup> ephemeris system provides the velocity of the Earth about the solar barycenter (including gravitational effects from planets and moons) with an impressive precision of about one millimeter per second.

The Doppler technique was the first method to detect planets around other stars. Latham *et al.* (1989) used Doppler velocity measurements to detect the first substellar mass object orbiting the star HD 114762. They interpreted this object as a likely brown dwarf since they derived  $M \sin i \sim 12M_{Jup}$  (Jupiter masses) for the companion. The object resides at the mass boundary between planets and brown dwarfs, however, the unknown inclination likely means that the true mass is in the brown dwarf regime. Planetary mass objects were found orbiting the neutron star PSR 1257+12 by Wolszczan and Frail (1992). This rapidly spinning neutron star was serendipitously oriented so that a narrow synchrotron beam swept across the solar system like a beam from a lighthouse. Careful monitoring of the pulsar timing permitted the detection of three planets that were just a few times the mass of the Earth. More than 20 years later, the precision of pulsar timing measurements still exceeds the precision that has been achieved with other Doppler techniques. A few years later, Mayor and Queloz (1995) detected the first planet around a Sun-like star. This was the beginning of an era of successful Doppler planet surveys (see the review by Fischer *et al.*, 2014).

The stellar radial velocity semi-amplitude  $K_*$ , can be expressed in units of  $\text{cm s}^{-1}$  as a function of the orbital eccentricity  $e$ , the orbital period  $P$  (in years), the combined stellar and planetary mass (in solar mass units), and the planet mass  $M_P \sin i$  (in units of Earth masses,  $M_\oplus$ ):

$$K_* = \frac{8.95 \text{ cm s}^{-1}}{\sqrt{1-e^2}} \frac{M_P \sin i}{M_\oplus} \left( \frac{M_* + M_P}{M_\odot} \right)^{-2/3} \left( \frac{P}{\text{yr}} \right)^{-1/3}. \quad (5.2)$$

Because only the projected line-of-sight velocity is measured, the inferred planet mass from Doppler measurements is  $M_P \sin i$ , the product of the true planet mass and the sine of the orbital inclination; the true mass of the planet cannot be determined. However, in a statistical sense the probability that the orbital inclination is within a particular range  $i_1 < i < i_2$  is given by:

$$\mathcal{P}_{incl} = |\cos(i_2) - \cos(i_1)|. \quad (5.3)$$

Thus, there is an 87% probability that orbital inclinations lie between  $30^\circ$  and  $90^\circ$ , implying that the true planet mass is statistically within a factor of two of  $M_P \sin i$  for the vast majority of Doppler-detected exoplanets.

<sup>1</sup> <http://ssd.jpl.nasa.gov/?ephemerides>

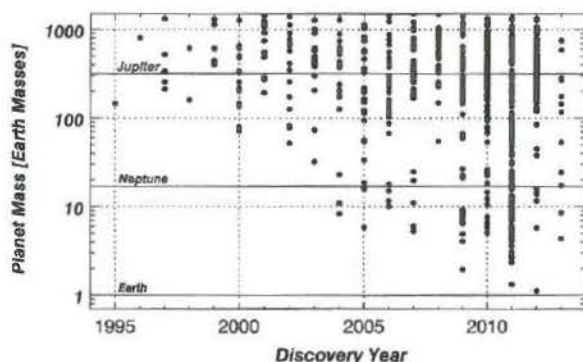


Fig. 5.3 Detection of exoplanets over time. Black dots indicate Doppler detections. Solid horizontal lines indicate the masses of Jupiter, Neptune and Earth.

In order to derive the orbital period and other orbital parameters, the radial velocity observations must span at least one complete orbit. Assuming circular orbits and a  $K_*$  corresponding to a given velocity precision (say,  $1 \text{ m s}^{-1}$ ), the minimum detectable mass can be calculated over a range of orbital periods to determine the threshold for the minimum detectable planet mass for the Doppler technique.

Figure 5.3 shows a time line of exoplanet detections; clearly the community has been addressing the technical challenges and improving the Doppler measurement precision so that the minimum detectable planet mass has been dropping over time. The data point close to one Earth mass indicates the companion to  $\alpha$  Cen B (Dumusque *et al.*, 2012) with an orbital period of 3.24 days. The question now is whether we can further improve the Doppler precision so that Earth analogs in habitable zone orbits can be discovered around nearby stars.

### 5.2.2 Current limitations to Doppler precision

The measurement of Doppler shifts induced by orbiting planets is technically challenging. In order to reach a Doppler precision of  $1 \text{ m s}^{-1}$  the wavelength must be known with a relative precision of at least  $10^{-9}$ , a nontrivial requirement. A Doppler shift corresponding to  $1 \text{ m s}^{-1}$  typically moves the stellar lines by less than 1/1000th of a pixel on a CCD detector. However, the spectrum will move on the detector for other reasons, too. Variations in the temperature, pressure, or mechanical flexures can shift the stellar spectrum by more than a pixel. Time-varying imperfections in the CCD can compromise the measurement of wavelength shifts. Contamination from a Moon-lit sky or a background star can induce spurious velocity signals. In short, everything matters and all of these issues must be controlled or tracked.

### 5.2.3 Stellar noise for Doppler techniques

Even if the technical and engineering challenges are perfectly managed, another threat to precise Doppler measurements remains outside of our control: coherent velocity flows on the surface of the star. Any technique that relies on observations of the host star to detect the unseen planet (Doppler, transits, astrometry, but not direct imaging or microlensing) will be affected by signals arising from the stellar photosphere. Planet hunters often refer to these signals as stellar noise. Of course, the stellar noise is signal to our colleagues who study the Sun and other stars; these signals include p-mode oscillations and features that are correlated with time-variable magnetic fields: variability in granulation, starspots, meridional flows (see chapters on the Sun and its magnetic activity listed in Table 1.2). The magnitude of these variable velocities can be hundreds of meters per second, making them important even if they are diluted by the integrated stellar flux.

In the case of p-mode oscillations, the variability has a typical period of a few minutes for stars like the Sun. The amplitude of the radial velocity signal from p-modes depends on whether the pressure modes are in resonance and is also a function of the spectral type of the star. However, radial velocities from typical p-mode signals usually have an amplitude that is no more than a few meters per second. By taking long or multiple exposures, it is possible to average over p-mode oscillations. From the perspective of the planet hunters, this high frequency contribution to errors is the least serious of the potential stellar noise sources.

Convective granules are a more significant source of stellar noise. In principle, what goes up must come down; however, the intensity of the hot upward flows is greater than the cool downward flows. This produces asymmetry in the spectral line. If the granulation were in a steady state, that asymmetry would not matter. However, magnetic fields cause a local suppression of granulation. Because the magnetic fields are time-variable, the granulation flows are variable and the spectral line profile will be time-variable. With high enough signal-to-noise and high enough spectral resolution, it may one day be possible to distinguish between the effect of stellar noise and Doppler shifts associated with the bulk motion of stars. Current instruments do not have that resolution, so the Doppler analysis code interprets this as a shift in the line centroid over time – i.e., a spurious net stellar bodily Doppler shift. The time scale for convective flows ranges from several minutes to a couple of hours, but the magnitude of this effect is difficult to assess.

Cool spots in the stellar photosphere also cause spectral line profile variations. As a spot emerges from behind the stellar disk as the star rotates, it blocks out light from the approaching limb of the star and the Doppler-broadened spectral line has less light in the blue wing. Later, the spot moves across the rotating star, and blocks light from the receding edge of the star; now the spectral line profiles all have less

intensity in the red wing. The Doppler code interprets these line profile variations as a net red shift followed by a net blue shift with a periodicity that matches the rotation period of the star. The rotation period of stars on Doppler planet surveys is uncomfortably close to the orbital periods of planets that we want to detect; this has led to confusion in the interpretation of data on more than one occasion. The spot signal is further complicated because it attenuates over a few rotation cycles and differential rotation and spot migration produces spots with slightly varying periods.

Longer-term magnetic activity variations, comparable to the solar cycle, have also been correlated with radial velocity variations. All of the above issues only represent “the devil that we know”. There are additional noise sources and velocity flows in stars that are less well understood, such as meridional flows. Current instruments do not have the ability to resolve most of the photospheric noise from Doppler shifts. Without new instrument designs and analysis techniques that have the ability to detect photospheric velocities, the Doppler technique will be limited to a precision of about  $1 \text{ m s}^{-1}$ .

### 5.3 Transit technique

In the lucky case where the orbit of a planet takes it along a path that crosses our line of sight to the star, the planet will block out a fraction of the stellar flux. The decrease in brightness scales with the ratio of the cross sectional area of the planet to the star (see Fig 5.4, reproduced from a review by Winn, 2011). Thus, if we can measure or estimate the radius of the star, we can easily calculate the size of the transiting planet.

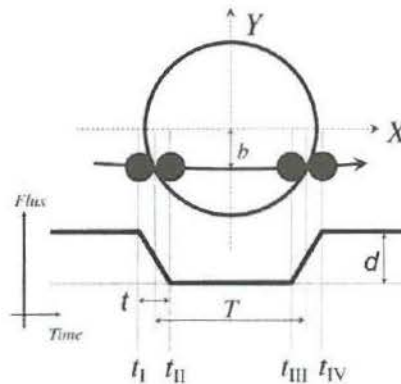


Fig. 5.4 The sketch of a transit light curve shows that the measured flux from the star begins to decrease during ingress. The flux is at a minimum after the planet has completed ingress and before the planet begins egress. After egress, the measured flux returns to the pre-transit value. Reproduced with permission from Winn (2011).

Transit observations uniquely provide a measurement of the radius of exoplanets for cases where the stellar radius is known. Ground-based transit observations only have the precision to detect gas giant planets; however, the spaced-based *Kepler* mission has detected thousands of planet candidates and confirmed planets with radii as small as the Earth. The real bonus comes when transit and radial velocity measurements can be combined to calculate an average density for exoplanets with masses comparable to or greater than Neptune. The technique is limited to a narrow range of essentially edge-on orbital configurations (inclinations close to  $90^\circ$ ) and to relatively short orbital periods (up to about 1 year). However, geometrical correction can be made to deduce the statistics of these planets. Thanks to the *NASA Kepler* mission, we now know that small rocky planets are far more common than gas giants.

The first transiting planet was detected around the Sun-like star HD 209458 (Henry *et al.*, 2000; Charbonneau *et al.*, 2000). In this case, the photometric monitoring of the star began after the planet was first discovered by the Doppler technique. Although the inclination was unresolved by the radial velocity measurements, the short period of this planet meant that the transit probability was about 10% (see Eq. (5.4)) and the other orbital parameters derived with Doppler data were used to predict the putative transit time. Because both the size and the mass of the planet were known (in the case of transiting planets, we know the inclination so the Doppler measurements yield a true mass for the planet, not just  $M \sin i$ ), the mean density of the planet was easily calculated. Density is a powerful characterization parameter that reveals information about the internal structure and atmospheres of exoplanets.

There are also programs that carry out nearly continuous photometric monitoring with the hope of a serendipitous transit observation. The HAT-NET (Bakos *et al.*, 2007), MEarth (Charbonneau *et al.*, 2009), and the XO Project (McCullough *et al.*, 2005) are examples of ground-based transit surveys. Examples of space-based missions that have been used to search for transiting planets include the Hubble Space Telescope (HST; Brown *et al.*, 2001), Spitzer (Knutson *et al.*, 2007a), CoRoT (Deleuil *et al.*, 2000) and *Kepler* (Borucki *et al.*, 2003).

In order for the planet to transit, the impact parameter ( $b$  in Fig. 5.4) must be less than unity, which corresponds to the angular radius of the star. In practice, this is a requirement for nearly edge-on inclinations; as shown in Fig. 5.5, most of the orbital inclinations for the planet candidates from the *NASA Kepler* mission are indeed between  $87^\circ$  and  $90^\circ$ . The ratio of the stellar radius to the semi-major axis  $a$ , or  $R_*/a$ , is also of fundamental importance in the geometry for transits. The probability that a given planet will transit is given by the following expression:

$$P_{tr} = 0.0045 \left( \frac{\text{AU}}{a} \right) \left( \frac{R_* + R_p}{R_\odot} \right) \left[ \frac{1 + e \cos(\pi/2 - \omega)}{1 - e^2} \right]. \quad (5.4)$$

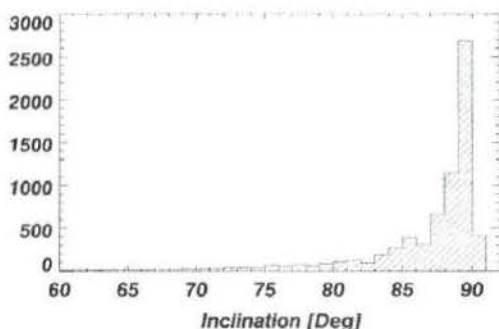


Fig. 5.5 The distribution of inclinations for the *Kepler* transiting planet candidates are highly biased toward edge-on ( $i = 90^\circ$ ) configurations (drawn from the list of KOIs in the NASA Exoplanet Archive).

This relation can be used to back out a geometrical correction for planet occurrence rates determined by transits. To appreciate the observational detection biases for the transit technique, it helps to assume circular orbits so that the last term in Eq. (5.4) reduces to unity. Then it is clear that for a given size of star, planets that have small semi-major axes and large radii are most easily detected.

Transiting gas giant planets uniquely permit studies of gas giant atmospheres. Although exoplanets cannot be spatially resolved from the star, it is possible to obtain a faint transmission spectrum of the exoplanet atmosphere, generally with low-resolution spectroscopy. Most transmission “spectra” are really spectrophotometric observations, obtained with broadband photometry (e.g., J, H, and K bands). The game plan is to obtain a transit light curve in each bandpass. Before the beginning of the transit, the only flux contribution is from the star. During transit, the flux in each bandpass is a combination of the flux from the star and the transmission spectrum of the planet. The light curve is then modeled in each bandpass, fitting for the ratio of the radius of the planet to the radius of the star and for limb-darkening (discussed below). This model of the planet radius provides three points for the planet’s transmission spectrum, in the broad J, H, K bandpasses. Extracting spectral information based on three (very low resolution) points is challenging; as a result, the detection of molecules such as  $\text{H}_2\text{O}$ ,  $\text{CO}_2$ , and  $\text{CH}_4$  and assessments about the thermal structure of atmospheres in hot and warm Jupiters and Neptunes can be controversial (Tinetti *et al.*, 2010; Crouzet *et al.*, 2012; Grillmair *et al.*, 2008; Barman, 2008; Madhusudhan and Seager, 2009).

Planets that transit their host stars are also occulted when they pass behind the star. The planet occultation is sometimes called a secondary eclipse and it provides a unique opportunity to obtain an isolated spectrum of the star. The stellar spectrum obtained during occultation can be subtracted from the unresolved combined spectrum of the star plus planet to yield a spectrum of the planet alone.

### 5.3.1 Limb darkening

The shape of the transit light curve provides information about the stellar atmosphere. When we look at the spherical star, it appears brighter and bluer in the center and redder near the edges or limb of the star. Both the density and temperature are decreasing as a function of the stellar radius. When we look near the edge of the star, we see down to an optical depth of  $\tau \sim 1$  but we are looking through a column of relatively cooler and lower density gas that is higher up in the stellar atmosphere. When we look at the center of the star, we also see down to an optical depth of  $\tau \sim 1$ ; however, this column of gas extends to deeper physical depths in the star and is therefore hotter and higher in intensity. Because of limb-darkening, a transiting planet will block more flux from the bright center of the star than near the edges.

A beautiful example is shown in Fig. 5.6, which is reproduced from Knutson *et al.* (2007b). Each of the transit curves was taken with a different bandpass using the Space Telescope Imaging Spectrograph (STIS) on the Hubble Space Telescope

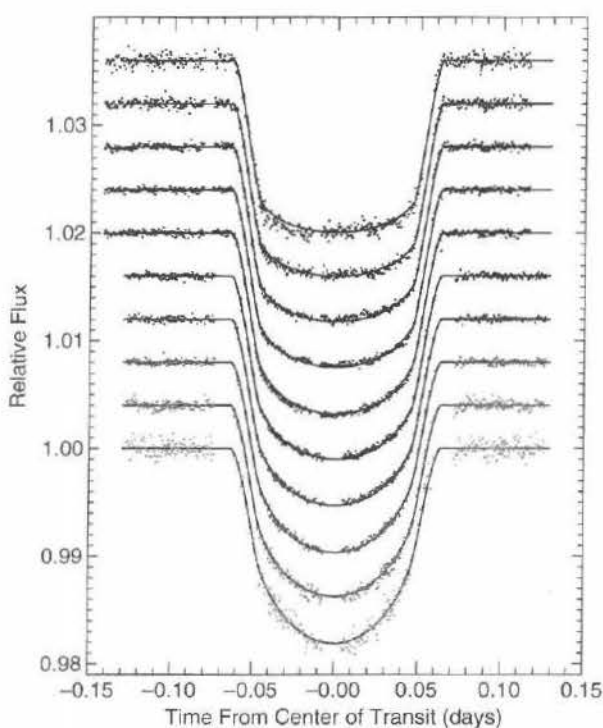


Fig. 5.6 Observations of HD 209458 in different HST bandpasses show the wavelength dependency of limb darkening (red wavelengths at top to blue at the bottom). (From Knutson *et al.*, 2007b).

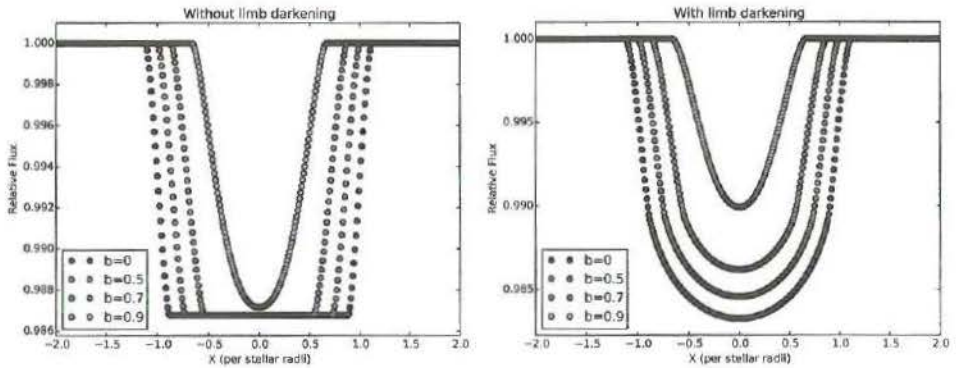


Fig. 5.7 Left: the shape of the transit light curve depends on the impact parameter  $b$  (from 0 to 0.9 from the outside inward in the diagram). Right: inclusion of limb darkening also affects the shape of the ingress and egress, making the curves more rounded. Figures courtesy of Meg Schwamb.

(HST). Limb darkening changes the shape of ingress and egress and the light curves are more rounded for the blue wavelengths of light than for the red wavelengths. Knutson *et al.* (2007b) used a nonlinear limb-darkening law to model the wavelength-dependent shapes of the transit curves in Fig 5.6.

Changing the impact parameter also affects the shape of the light curve because it changes the duration of the transit. At an impact parameter of zero, the planet is perfectly aligned with the diameter of the star and the maximum transit duration occurs. When the impact parameter is close to unity, only a grazing transit is observed. Figure 5.7 (left) shows the difference in the shape of the transit curve for different impact parameters without considering limb darkening. In this figure, the same wavelength bandpass was assumed for all four (synthetic) light curves.

If limb darkening is included, there is an additional change in the shape of ingress and egress for the curves, and Fig. 5.7 (right) shows a more realistic set of transit curves for impact parameters of 0, 0.5, 0.7, and 0.9. Although both the impact parameter and limb darkening will change the shape of the transit curve, these effects can be distinguished because the impact parameter is wavelength independent.

### 5.3.2 Stellar noise for transit techniques

As with Doppler observations, the flux for transit measurements comes from the host star. Therefore, starspots can be a source of additional noise. The cooler starspots result in a diminution of flux (especially at bluer wavelengths). When a planet crosses a starspot, the sum of the flux decrement from the transit plus the starspot is not as great and the star brightens slightly. The shape of the photometric

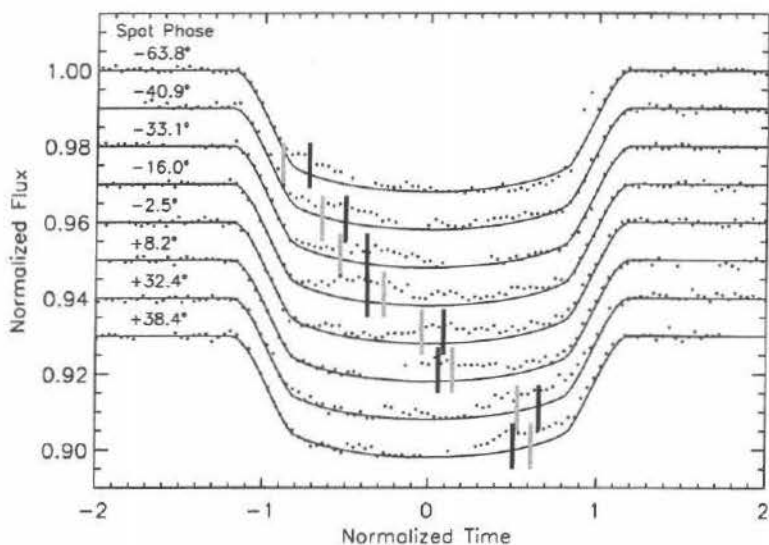


Fig. 5.8 As the planet in CoRoT-2 transits starspots on HD 189733, which are cooler than the rest of the star, less flux is blocked. The rotation period of the planet is different from the rotation period of the spots, and the spots advance in this time series of transit light curves. These data were cleverly used to determine the alignment of the planet with the equatorial plane of the star (reproduced from Nutzman *et al.*, 2011).

perturbation to the light curve depends on the relative size of the planet and spot and the relative spot temperature. This effect can be seen in Fig. 5.8 for the CoRoT-2 transiting planet (Nutzman *et al.*, 2011). For this star, the rotation period is roughly 4.5 days and the typical spot lifetime is about 55 days. The orbital period of the planet is only 1.74 days, so as the planet circles around, the spot cluster has advanced slightly on the star.

### 5.4 Direct imaging

The majority of exoplanets that have been detected are within 5 Sun–Earth distances (AU) of their host stars. This is due to the detection biases of the two predominant exoplanet detection techniques, the Doppler technique and the transiting method. The direct imaging technique offers the most promising prospect to detect gas giant exoplanets in wide orbits. The opportunity to directly image an exoplanet has enormous appeal. With enough photons from the planet, one day in the future it might be possible to see clouds rotating on the surface of the planet or to take a spectrum of the exoplanet atmosphere from a direct image.

A 10-m telescope imaging at H band has a 32-milliarcsecond diffraction limit. Such an instrument has sufficient spatial resolution to detect a planet on a 5-AU orbit around a star at 150 pc, approximately the distance to the Orion star-forming

region (Oppenheimer and Hinkley, 2009). However, scattered light from the star generally prevents the detection of planets at small angular separations. The critical requirement for direct imaging is high contrast, the brightness ratio between a planet and its host star. This requirement is less severe for wider angular separations where scattered light from the star is less intense. While the contrast requirement for imaging a young and hot Jovian planet is  $10^{-8}$ , the prototypical high-contrast observation of GL 229 B with a relatively wide angular separation was detected with a contrast of only  $10^{-4}$  (Oppenheimer, 1999; Oppenheimer *et al.*, 2001).

Improvement of image reduction techniques will enable direct exoplanet detections in more systems, for example, HR 8799 (Marois *et al.*, 2008), Fomalhaut (Kalas *et al.*, 2008), and  $\beta$  Pictoris (Lagrange *et al.*, 2010). With the advent of next generation adaptive optics systems, instruments such as the Gemini Planet Imager (Macintosh *et al.*, 2006), the Project 1640 (Hinkley *et al.*, 2008), and SPHERE (Dohlen *et al.*, 2006) will deliver better than  $10^{-10}$  contrast close to the diffraction limit of a telescope. These instruments will not only image young Jovian planets but also obtain low-resolution spectra to study their atmosphere.

### 5.5 Microlensing

The microlensing technique was developed to search for dark matter in the form of massive compact halo objects, or MACHOs. The method works in the following way: the light from a distant source brightens when a “lensing” star passes between the line of sight of the observer and the background source. The lensing star warps spacetime through the mathematical construct of an Einstein ring; light from the source bends around the lensing star and the observer detects more photons. The duration of the photometric brightening (i.e., the microlensing event) is a function of the mass of the lens star; however, the brightening amplification depends almost entirely on the impact parameter (the alignment of three objects: the observer, the lens, and the source).

The brightening amplification is remarkably insensitive to the mass of the lens. Even low mass planets (in orbit around the lensing star, or free-floating planets) can induce strong amplification of the source starlight if the alignment is good. This is what makes the technique useful for the detection of low mass exoplanets, when they orbit at angular separations near the Einstein Ring.

A historical challenge for microlensing detections has been the follow up observations required to search for the lens star. Because 70% of the stars in the galaxy are M dwarfs, the lensing star is likely to be faint and difficult to recover, making the detection more difficult to characterize. However, the microlensing community is tightly organized with observing stations at all latitudes on the Earth and rapid response follow-up. The recovery rate of the lensing stars has improved and clever new techniques are being developed to measure microlensing parallaxes, yielding

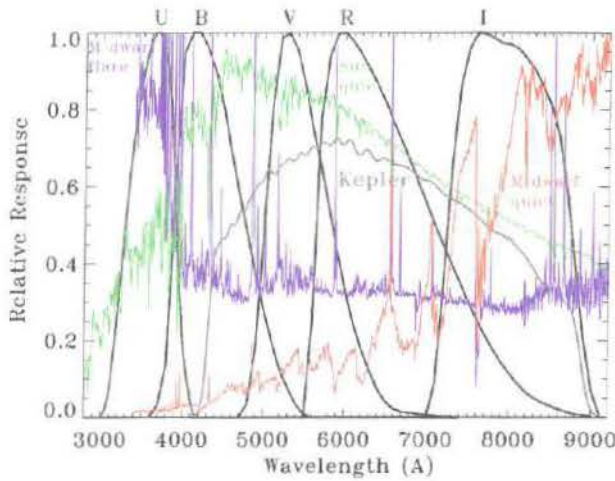


Fig. 2.5 Wavelength coverage of several standard filters used in optical astronomy, along with the wavelength coverage of the filter used in the Kepler mission. Overplotted are also spectral energy distributions of a quiescent and flaring M-dwarf atmosphere, taken from Kowalski *et al.* (2013). The solar spectrum is the 1985 Wehrli Standard Extraterrestrial Solar Irradiance Spectrum from <http://rredc.nrel.gov/solar/spectra/am0/>.

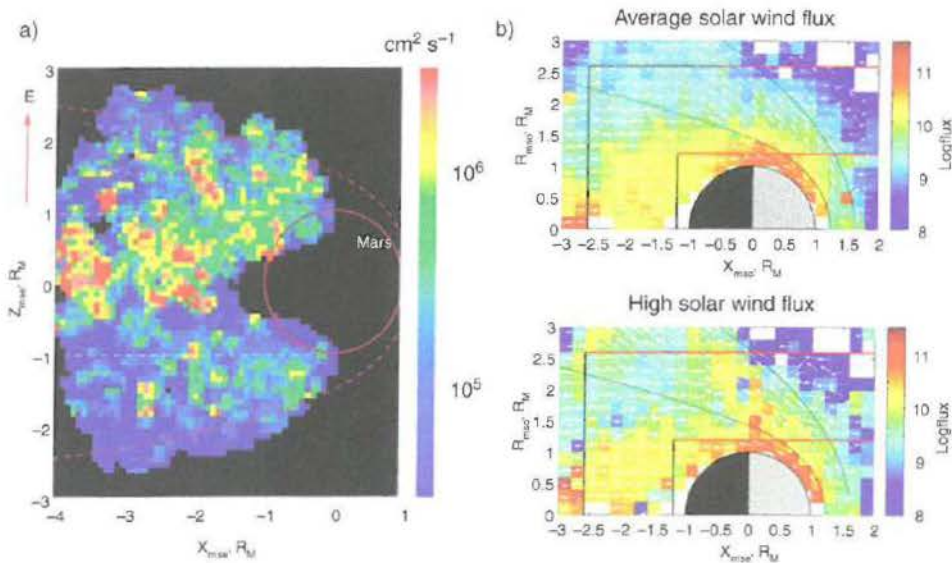


Fig. 7.6 Ion escape from the Martian atmosphere, organized by solar drivers. The Sun is to the right in both panels. (a) Escaping ion fluxes downstream from Mars are greater in the hemisphere of upward directed (with respect to the planet) solar wind electric field (Barabash *et al.*, 2007); (b) escaping ion fluxes downstream from Mars are greater during periods of high solar wind flux. (From Nilsson *et al.*, 2011.)

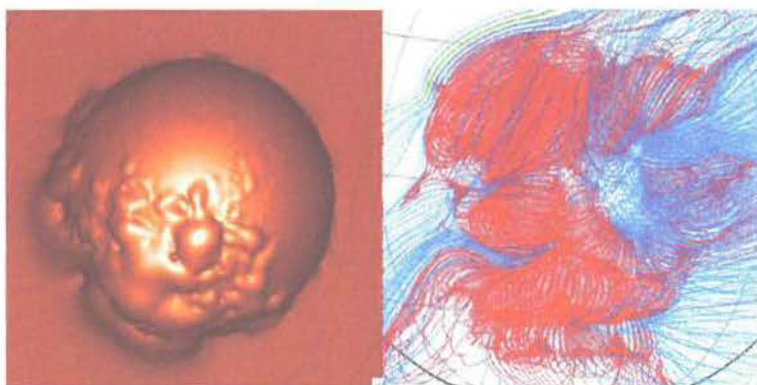


Fig. 7.8 Influence of magnetic fields on planetary near-space environments. Magnetic fields supply magnetic pressure (left: for Martian crustal magnetic fields) that deflect solar wind, but also modify magnetic topology (from Brain, 2006); (right: for the strong Martian crustal fields in the southern hemisphere, where red denotes closed field lines and blue denotes field lines open to the solar wind at one end) that enable exchange of particles and energy between the atmosphere and solar wind. Both renderings result from model calculations that include contributions from crustal fields and external drivers (solar wind or IMF).

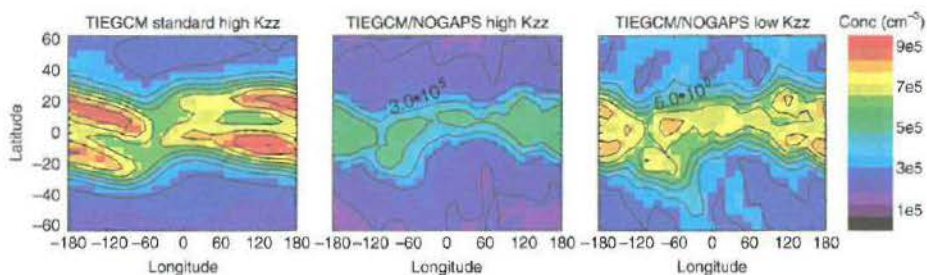


Fig. 9.11 Calculated averaged peak  $F_2$  electron density for March, 1300 local for three TIEGCM simulations. Left column uses standard  $K_{zz} = 125 \text{ m}^2 \text{ s}^{-1}$  with vertical winds from the right column of Fig. 9.7. Middle uses NOGAPS-ALPHA vertical winds. Rightmost field is with NOGAPS-ALPHA vertical winds and  $K_{zz}$  divided by 5.

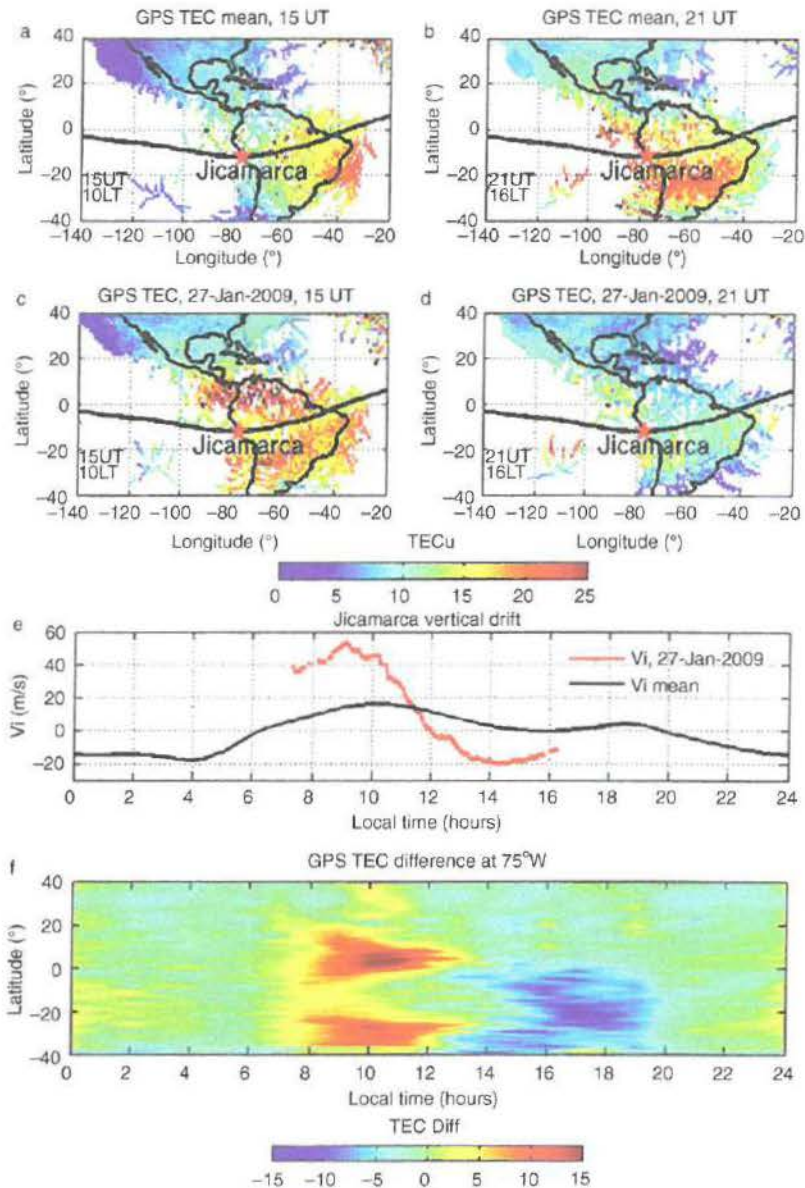


Fig. 9.12 Perturbations to the ionosphere, both total electron content (TEC) and vertical ion drift from the sudden stratospheric warming (SSW) of January 2009. The top row shows typical morning (15 UT = 10 local time at 75° W) and afternoon (21 UT) TEC fields over South America. The second row shows these fields after the SSW with a notable enhancement of TEC in the morning. The third panel shows the difference in the vertical ion drift as measured from Jicamarca Peru. The bottom panel shows difference fields between the SSW perturbation and the mean case as a function of local time, emphasizing the morning TEC enhancement and the afternoon depletion. (From Goncharenko *et al.*, 2010.)

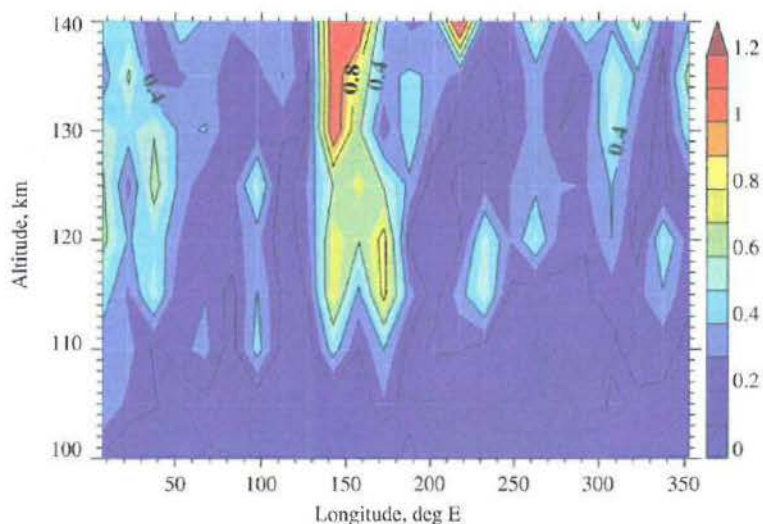


Fig. 9.14 Density variance data from the Mars Odyssey accelerometer in  $15^\circ$  and 5-km bins as function of longitude over about 127 orbits. (From Fritts *et al.*, 2006.)

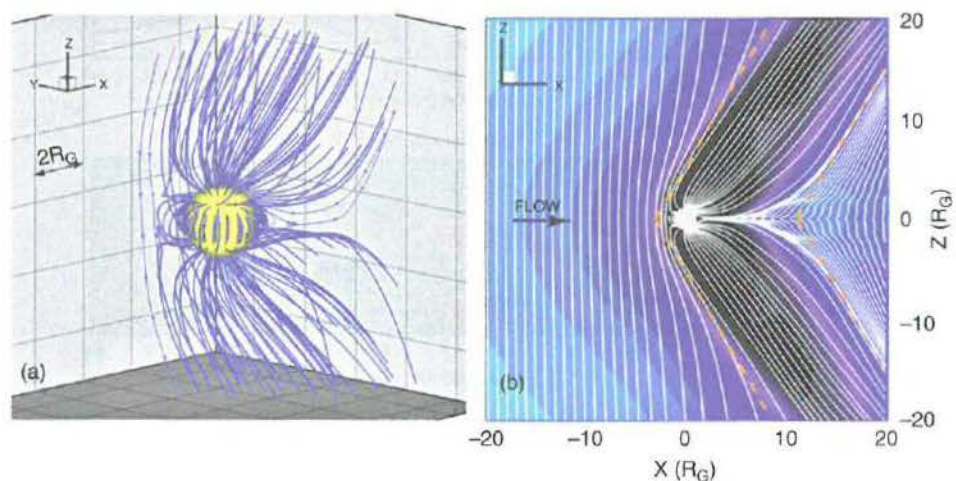


Fig. 10.5 (a) Selected magnetic field lines in Ganymede's magnetosphere from an MHD simulation. (b) Magnetic field lines projected onto the  $x-z$  plane at  $y = 0$ . The  $x$ -component of the plasma flow velocity is shown in color. Orange dashed lines are tilted relative to the background field at the Alfvén angle and the flow is excluded from regions downstream of the left hand dashed lines, reappearing only in regions about  $5 R_G$  further downstream. In the simulation, the sphere of radius  $1.05 R_G$  is the inner boundary for plasma flow. (From Jia *et al.*, 2008.)

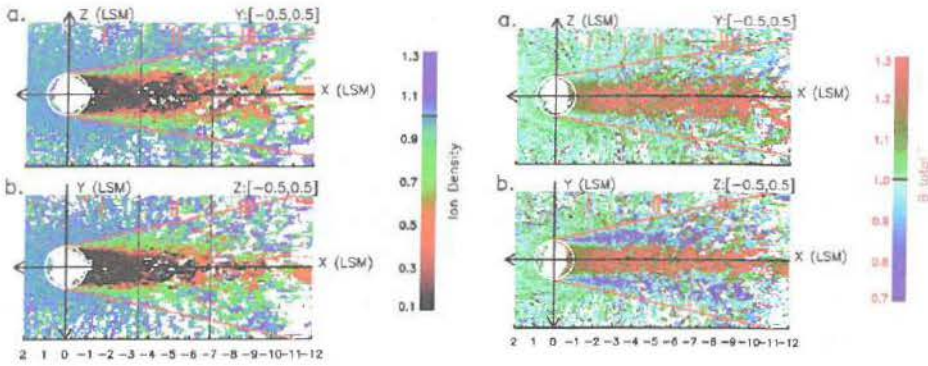


Fig. 10.7 Ion density (left) and magnetic field (right) in the vicinity of Earth's Moon from measurements by the *Artemis* spacecraft. The parameters represented by color are normalized by their values in the upstream solar wind. The  $x$ -axis is antiparallel to the solar wind flow. The data are plotted in the  $x-z$  plane which is the plane of the solar wind field and the flow, and in the  $x-y$  plane, perpendicular to this plane. The red lines diverging in the direction of negative  $x$  denote the wake boundary across which the density changes significantly. The divergence from the wake center is controlled by the propagation of fast mode waves. (From Zhang *et al.*, 2014.)

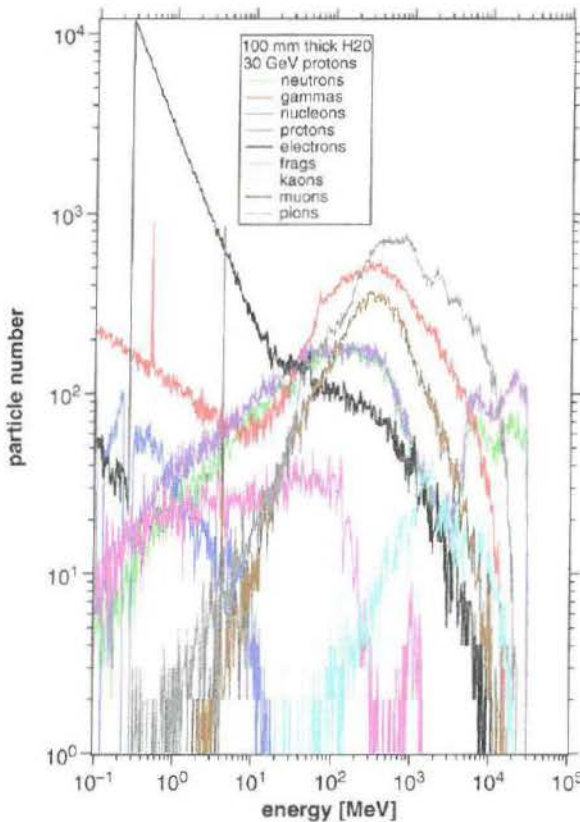


Fig. 12.11 Galactic cosmic-ray spectra for various particle populations. (Diagram provided by D. Haggerty, JHUAPL.)

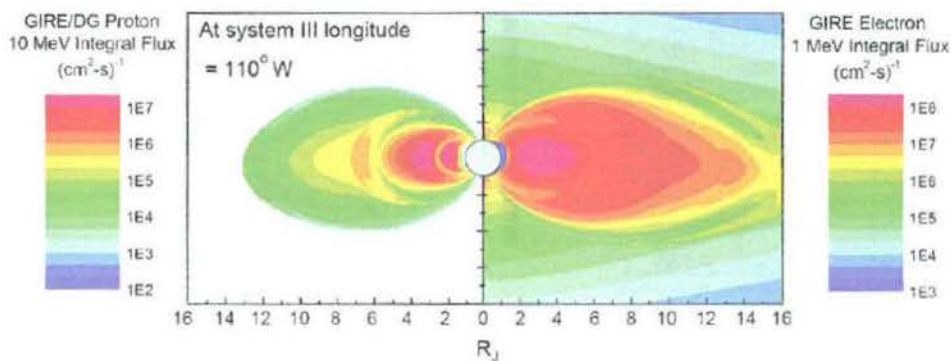


Fig. 12.12 Two-dimensional integral flux distributions for electrons (right section) and protons (left section) at Jupiter based on the Divine-Garrett/GIRE radiation models. (From Paranicas *et al.*, 2009.)

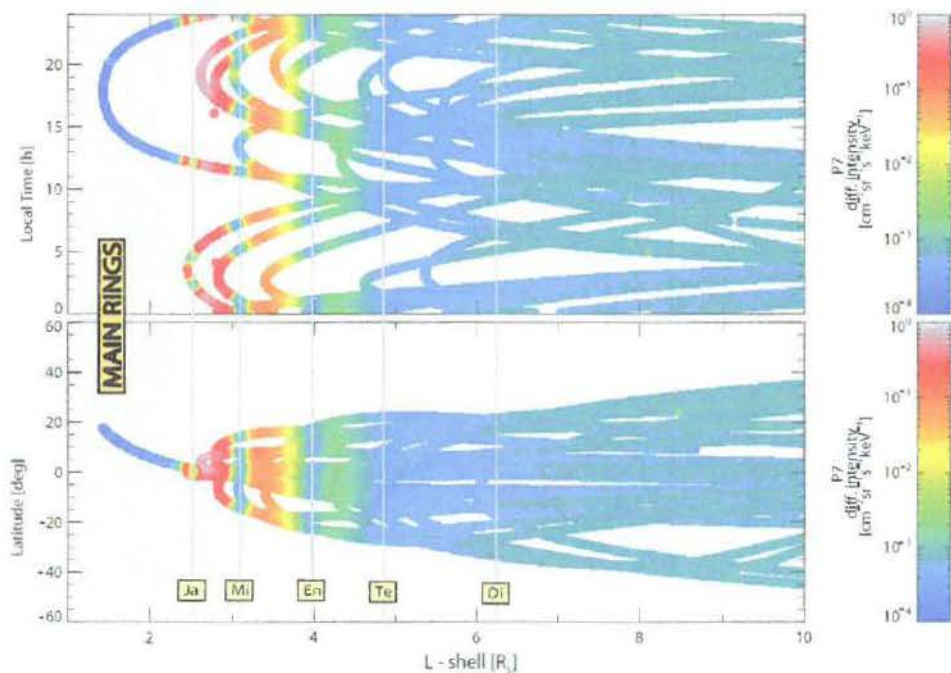


Fig. 12.13 Macrosignatures of energetic ions in the inner magnetosphere of Saturn as a function of L-shell and either local time (upper panel) or latitude (lower panel). Color-coded are the differential intensities of ions ( $> 10$  MeV/nucleon) as measured between 2004 and 2007 by the Low Energy Magnetospheric Measurement System LEMMS onboard the Cassini spacecraft. (From Roussos, 2008.)

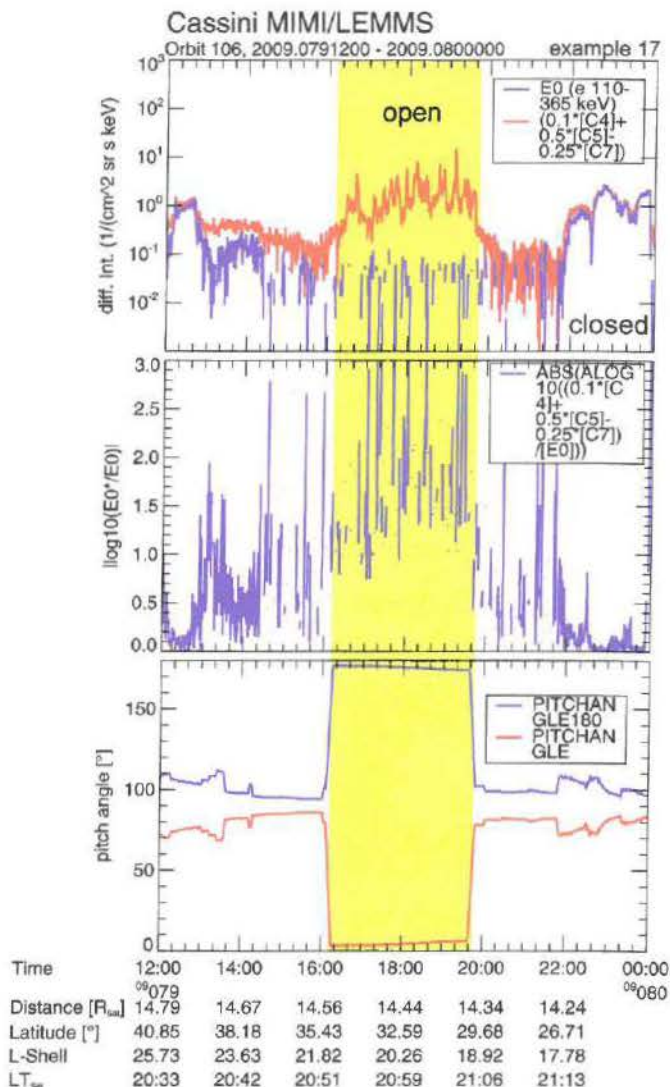
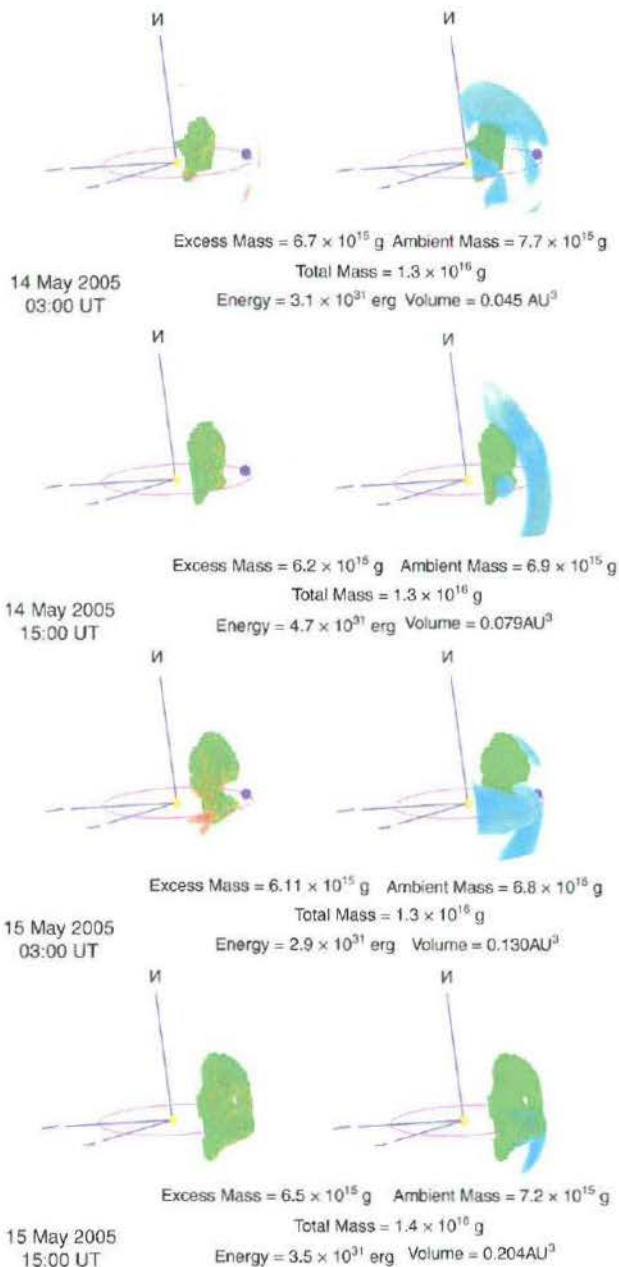


Fig. 12.16 Intensity of electrons along and against the magnetic-field direction inside Saturn's magnetosphere.

Caption for 13.10 (overleaf)

The 3D CAT reconstructed visualization of the distribution of solar-wind density upwards of  $8 e^{-} \text{cm}^{-3}$  (brighter colors toward yellow mean increasing density) on the left-hand side and high-velocity portions (blue) on the right-hand side showing the developing and changing reconstructed structure of the 13–15 May 2005 coronal mass ejection (CME) event sequence. The left-hand density images are highlighted with green cubes to encompass the reconstructed volume of the mass portion of the CME. This same highlighted volume is depicted on the



Caption for 13.10 (cont.)

right-hand velocity reconstructions for illustrative purposes. Each image is labeled with the masses, volume, and energy values on each date and time as shown. All non-CME-related features have been removed for clarity of viewing when displaying the 3D volume. The axes are heliographic coordinates with  $X$ -axis direction pointing toward the vernal equinox, and  $Z$ -axis directed toward solar heliographic North. An  $r^{-2}$  density increase has been added to better show structures further out from the Sun (the central sphere) to the Earth (the blue sphere) along with the Earth orbit (ellipse). (From Bisi *et al.*, 2010a.)

distances and masses of the lensing object with a few astrometric and photometric ground-based observations.

This technique will be particularly powerful for determining exoplanet masses when WFIRST (the highest-ranked project in the 2010 Astronomy Decadal Survey) is launched. If parallaxes can be recovered for most of the WFIRST detections, it will make this technique a game-changer. Microlensing will become a powerful technique for detecting exoplanets at separations beyond the ice line and for understanding exoplanetary architectures.

## 5.6 Astrometry

Astrometry is one of the oldest techniques and has been used to measure stellar parallaxes, proper motions, and binary star orbits. With this technique, the changing position of the star in the plane of the sky is measured with respect to other objects – typically background stars. Like the Doppler technique, at least one full orbital period must be observed to map out exoplanet orbits. However, this technique recovers the full three-dimensional orbit, so there is not the  $M \sin i$  degeneracy of the Doppler technique.

Attempts to detect exoplanets with ground-based astrometry have been challenging because the center of mass for a star–planet system is generally inside the radius of the star. As a result, the photometric centroid barely moves. Astrometry is better leveraged for planets at large separations because the center of mass moves outside of the star. However, these planets also have longer orbital periods and the astrometric precision must be maintained for years.

In all cases, the astrometric wobbles induced by orbiting planets are tiny and it is an enormous challenge to identify background reference stars that do not move. Some improvement in ground-based astrometric precision have been realized with the use of adaptive optics to shrink the twinkling star. However, astrometry is best carried out above the Earth's atmosphere. The Hipparcos mission operated from 1989 to 1992 with a measurement precision of 1 milliarcsecond. Astrometry is about to undergo a new revolution. The European Space Agency (ESA) launched the Gaia mission in 2013. This mission will make the largest and most precise three-dimensional map for a population of more than one billion stars in the Milky Way galaxy. The collecting area of the Gaia telescope is 30 times the size of Hipparcos and the positional accuracy and proper motion measurements for most stars will be improved by a factor of 200.

## 5.7 Comparative planetology

### 5.7.1 Exoplanet formation

How do all of the exoplanet detections fit with our understanding of the formation and evolution of the solar system? The solar nebula theory provides a theoretical

description for the formation of the solar system. Indeed, it has been said that this model is so elegant, that it is hard to imagine that it could be wrong. The solar nebula theory neatly explains most observations: the planets closest to the Sun form in a hot environment and as a consequence these planets are small and comprised of refractory elements (i.e., elements whose solid state withstands high temperatures); the more massive gas giants form beyond the ice line (a distance where it is cold enough for dust grains to be coated with icy mantles) where the feeding ground is more voluminous; jovian planets have moons that were either captured or that form as mini-solar-systems; the planets all orbit in the same direction in the disk because they inherit the same angular momentum vector; the solar system is littered with leftover debris such as asteroids and comets. The theory supports the idea first suggested by Kant and Laplace that the proto-Sun was surrounded by a primordial spinning disk of dust and gas. All of the material that makes up the Sun drained through this disk.

Note that the primordial or protoplanetary disks are different from reprocessing disks or debris disks, which can be observed around older main sequence stars. Debris disks are caused by collisions of small bodies in the disk at later stages and can even be detected around old main sequence stars. Debris disks are dusty, gas-poor structures that evolve and dissipate with Poynting–Robertson drag (Wyatt, 2008) as stellar radiation causes dust grains to lose energy and spiral inwards.

The study of protoplanetary disks has made tremendous advances in parallel with the discovery of exoplanets. Lada and Wilking (1984) inferred the presence of dusty shells around young stellar objects (YSOs) in Ophiuchus based on an excess of infrared flux; light from the star that was trapped and scattered by dust particles. Their classification of three different types of YSOs suggested evolutionary stages. However, the geometry of the dust distribution was not actually observed until the refurbished Hubble Space Telescope (HST) resolved flattened pancake-shaped structures around young stars in the Orion Nebula (O'dell and Wen, 1994). However, observations cannot yet see into the protoplanetary disks because the disks are optically thick at most wavelengths. It is only the outer regions (beyond  $\sim 40$  AU) where the disk becomes optically thin to millimeter wavelengths that observations are secure. Thus, theory currently outpaces observational evidence about the temperature and pressure structure and the evolution of protoplanetary disks, a situation which should improve with data from the Atacama Large Millimeter Array (ALMA).

The mass of the protoplanetary disk is a fraction of the stellar mass and evolves with the central star. Our understanding of the physics and chemistry of protoplanetary disks is distilled in Fig. 5.9. The temperature is about 1500 K near the inner part of the disk and along the flared outer layers. These high temperature are too hot for grain growth, but a few AU from the protostar the disk mid plane

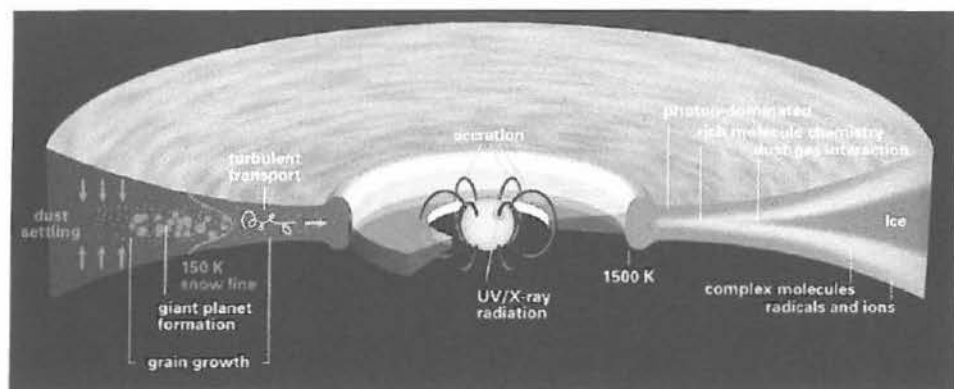


Fig. 5.9 A sketch of the structure and processes of protoplanetary disks. From a talk by Dmitry Semenov PPVI (Henning and Semenov, 2013; <https://www.youtube.com/watch?v=F2IDOccNy8c>).

is cool enough for icy grains to stick and grow. The opacity of the disk is set by the dust, which gradually decouples from the gas and settles toward the mid plane, increasing transparency of the disk over time.

Protoplanetary disks provide the initial conditions for planet formation. The formation of gas-giant planets was described in a seminal paper by Pollack *et al.* (1996). In the first phase of planet formation, the planet grows by runaway accretion of solid material. The second phase of growth is very slow; both solid and gas accretion are nearly time independent and this phase sets the planet formation time scale. Once the planet core reaches a mass of about  $10M_{\oplus}$ , the third phase of runaway gas accretion begins, growing the planet mass from ten to a few hundred  $M_{\oplus}$ . Pollack *et al.* (1996) estimated that gas-giant planet formation should take roughly 10 Myr. However, observations of protoplanetary disks in the 1990s presented a conundrum: the primordial disks appear to be nearly ubiquitous around stars that are 1 Myr; at 2 Myr only about half of young stars have disks and, by 10 Myr, the disks are essentially gone. Figure 5.10 shows the fraction of protoplanetary disks found in young cluster stars (Mamajek, 2009).

One triumph that emerged from the discovery of exoplanets was a solution to the disagreement between theory and observations for the formation time scale of gas-giant planets. The first detected gas-giant planets orbited close to their host stars providing evidence that exoplanets could undergo orbital migration. Thus, planets were not restricted to a planetesimal feeding ground at a fixed orbital radius; instead, the planet embryos are pushed around in the disk by planet–planet interactions and tidal torques. The access to a wider part of the disk suggests a wider feeding zone for more rapid accretion of planetesimals that would shorten the second phase of gas-giant planet formation described by Pollack *et al.* (1996).

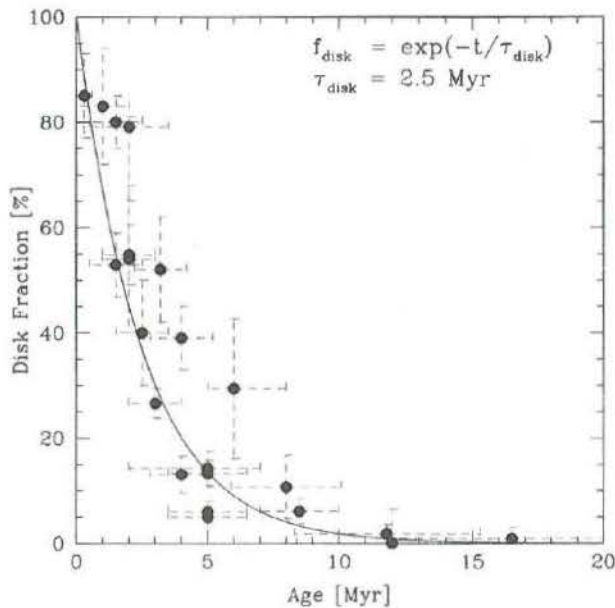


Fig. 5.10 Primordial disk fractions of stars in young clusters (Mamajek, 2009). These observations show that the dust disks last for only a few million years.

### 5.7.2 Exoplanet migration

The realization that exoplanets are mobile during the early stages of formation has led to many studies of dynamical interactions. The details of migration and the parking mechanisms that place gas-giant planets just a few stellar radii away from their host stars are an active area of research (Lin *et al.*, 1996; Batygin, 2012). In the younger primordial disk with significant gas and dust density, the planet embryos will clear gaps in the disk. In this case, material can pile up at both the inner and outer edges of the gap. When the disk mass at the edges of one of these gaps is comparable to the mass of the planet embryo the disk will exert a torque that causes the planet to migrate. The outer edge of the disk causes inward migration while the inner edge of the disk can produce outward migration. When multiple planet embryos exist in the disk it is possible for the outer embryo to become locked into a resonant orbit with the inner planet, a process called convergent migration. As the disk clears, convergent migration can leave planets in resonant orbits that persist stably over the lifetime of the star. This effect is especially powerful for resonances where the ratio of the orbital periods ( $P_{\text{outer}}/P_{\text{inner}}$ ) is close to an integer number,  $N$ . Planets with small  $N$  are said to be in mean-motion resonance (MMR) and the exchange of angular momentum between MMR planets is flagged by oscillations in eccentricity and orbital periods.

Another way to push exoplanets inward is through gravitational encounters. There are several proposed mechanisms that excite orbital eccentricity including secular migration (Wu and Lithwick, 2011), planet–planet scattering (Ford and Rasio, 2008; Nagasawa *et al.*, 2008), and Kozai perturbation in which gravitational interactions result in coupled variations in orbital inclination and eccentricity (Wu, 2003; Fabrycky and Tremaine, 2007; Naoz *et al.*, 2011). High-eccentricity planets with a small enough periastron passage eventually experience tidal circularization and can end up in short-period orbits.

Different migration mechanisms predict distinct observables. A particularly interesting observable is stellar obliquity, the relative angle between the stellar rotation vector and the vector of planet orbital plane. The stellar obliquity can be measured by observing the Rossiter–McLaughlin (RM) effect (Rossiter, 1924; McLaughlin, 1924). The RM effect is caused by a transiting object blocking some of the light from a rotating star. First, the planet crosses the approaching limb of the rotating star, decreasing the contribution of blue-shifted light in the spectral line and a few hours later the planet crosses the receding limb of the rotating star, decreasing the contribution of red-shifted light. The systematic decrement of Doppler-shifted light in the composite spectral lines results in a distortion of line profile, which is (mis)interpreted as a change in the radial velocity of the star. The shape of the RM curve during transit is entirely dependent on the stellar obliquity. Consequently, the stellar obliquity is determined by modeling the anomalous radial velocity signals during a transiting event.

Disk-driven migration is expected to produce a small stellar obliquity whereas gravitational encounters that temporarily pump up the orbital eccentricity of gas-giant planets should result in a wide range of stellar obliquities including retrograde orbits. The latter has been observed for many transiting planets (Winn *et al.*, 2010; Albrecht *et al.*, 2012) suggesting that high-eccentricity mechanisms drive gas-giant planets inward. However, it has also been suggested (Batygin, 2012) that the observed stellar obliquity range may reflect a primordial stellar obliquity due to interactions between protoplanetary disk and a companion star. Interestingly, the small stellar obliquity of low-mass multi-planet systems suggests well-aligned vectors for the stellar spin and planetary orbits (Sanchis-Ojeda *et al.*, 2012; Albrecht *et al.*, 2013). It is certainly possible that gas-giant and low-mass planets migrate by different mechanisms.

In summary, the most important revisions to the solar-nebula model and our understanding of planet formation can be attributed to one source: the addition of dynamical interactions between planets and the primordial disk. These dynamical interactions speed up the accretion time scales, produce mean-motion resonances, scatter planets out of the disk into non-coplanar orbits that can be detected by the Rossiter–McLaughlin effect and even eject some planets.

Several other studies have also suggested an important transition at  $\sim 1.5\text{--}1.7$  Earth radii. Rogers (2014) applied a hierarchical Bayesian statistical method for a sample of *Kepler* planets with determined mass and identifies a transition radius above  $1.6R_{\oplus}$ . Lopez and Fortney (2014) model radii for planets with mass between  $1\text{--}20M_{\oplus}$  considering different compositions and suggest a physically-motivated transition radius at  $1.75R_{\oplus}$ . Buchhave *et al.* (2014) study the metallicity distribution of 406 *Kepler* planet host stars. They find two characteristic planet radii ( $1.7$  and  $3.9R_{\oplus}$ ) that divide planets into three populations: terrestrial planets, gas-dwarf planets, and gas-giant planets.

Both the mass–radius relationship and the transition radius from rocky to non-rocky planet help us to better understand the formation history of small planets. Planets that form in-situ in the inner part of the disk would consist primarily of rocky materials and possibly a primordial H/He atmosphere (Chiang and Laughlin, 2013). In comparison, planets that have undergone significant migration should contain more volatile materials such as astrophysical ice ( $\text{H}_2\text{O}$ ,  $\text{CO}$ , and  $\text{NH}_3$ ). The debate of whether *Kepler* close-in planets form in-situ (Chiang and Laughlin, 2013; Hansen and Murray, 2013) or migrate (Swift *et al.*, 2013; Schlichting, 2014) should eventually gain evidence from studies of exoplanet atmospheres that add constraints on their chemical composition.

### 5.7.3 Exoplanet geology

Thousands of planet candidates were discovered by the *Kepler* mission, allowing for precise measurements of exoplanet radii. The combination of the radius and mass measurements (either from the Doppler technique or from transit timing variations) provide a mean density for hundreds of exoplanets and allow us to begin considering the bulk composition of unseen planets that orbit stars hundreds of light years away from us. The varying bulk composition of exoplanets results in different curves that cut through the mass–radius parameter space shown in Fig. 5.11.

Planets with radii smaller than 4 times that of the Earth can exhibit a remarkable diversity of compositions (Rogers and Seager, 2010). Weiss and Marcy (2014) considered the *Kepler*-detected planets with radii smaller than 4 times that of the Earth. Although their Doppler precision was not sufficient to measure reflex velocities from these small planets, they were able to place statistical limits on the exoplanet masses. They found that these small planets could be divided into two radius regions. Planets smaller than 1.5 Earth radii increase in density with increasing radius and seem to have a composition that is consistent with rock. Planets with radii between 1.5 and 4 times the radius of the Earth showed decreasing density with increasing radius, suggesting that the larger planet radius was a product of gaseous envelopes. Weiss and Marcy (2014) also concluded that the significant

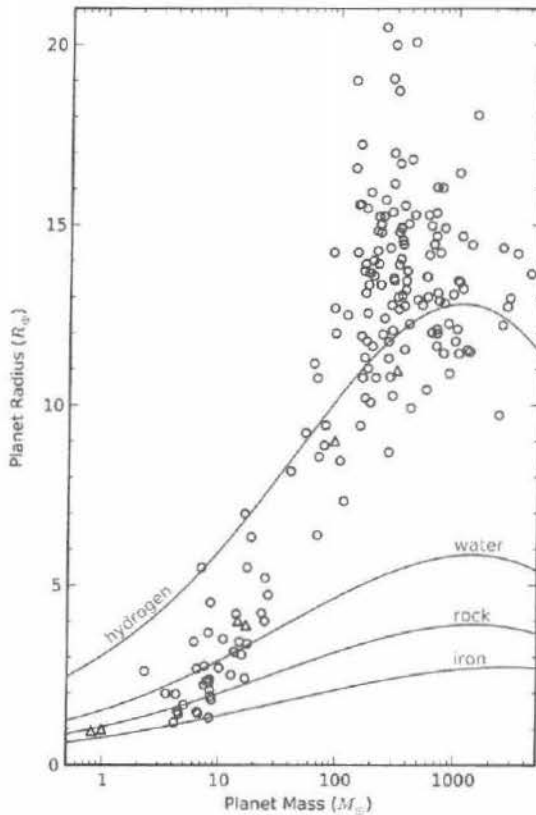


Fig. 5.11 Masses and radii of well-characterized exoplanets (circles) and solar-system planets (triangles). Curves show models for idealized planets consisting of pure hydrogen (Seager *et al.*, 2007), water, rock ( $\text{Mg}_2\text{SiO}_4$ ), or iron. (From Howard *et al.*, 2013).

amount of scatter in the mass–radius parameter space suggested a large diversity in planet composition at a given radius.

#### 5.7.4 Exoplanet statistics

With thousands of exoplanets and exoplanet candidates, it is possible to carry out statistically significant studies of the attributes of exoplanets. It is common to plot exoplanet mass as a function of orbital period when showing the distribution of exoplanets. However, that figure simply reflects the observational incompleteness and biases of the detection techniques and does not contain very much fundamental information about exoplanets.

However, there are other correlations that do reveal fundamental information. One of the first observed statistical correlations established that gas-giant planets

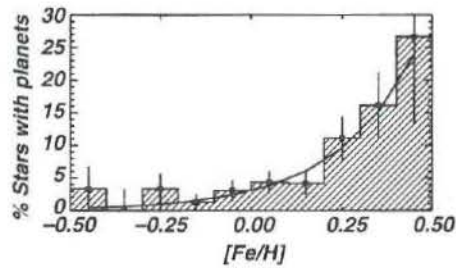


Fig. 5.12 High metallicity stars are more likely to host gas-giant planets than sub-solar metallicity stars. Figure from Fischer and Valenti (2005).

form more frequently around metal-rich stars (Gonzalez, 1997; Santos *et al.*, 2004; Fischer and Valenti, 2005, Johnson *et al.*, 2010). This planet-metallicity correlation was used as evidence for core accretion as the formation mechanism for gas-giant exoplanets that orbit closer than a few AU around their host main-sequence stars (see Fig. 5.12).

Interestingly, a similar correlation with host-star metallicity has not been identified for smaller Neptune-like or rocky planets (Sousa *et al.*, 2008; Neves *et al.*, 2013). The discovery of so many small planets with the *Kepler* mission has enabled a more thorough search. Buchhave *et al.* (2012) measured metallicity for a sample of 152 *Kepler* planet stars hosting planets with radii smaller than the radius of Neptune ( $4R_{\oplus}$ ) and did not find a metallicity correlation. Everett *et al.* (2013) obtained spectra of 220 faint *Kepler* planet host stars and reached a similar conclusion. Buchhave *et al.* (2014) then expanded their metallicity measurements to include 406 *Kepler* planet host stars. In their recent data, the average metallicities for gas-giant planets ( $R_p > 3.9R_{\oplus}$ ) and gas-dwarf planets ( $1.7R_{\oplus} < R_p < 3.9R_{\oplus}$ ) are above the solar metallicity ( $0.18 \pm 0.02$  dex and  $0.05 \pm 0.01$  dex), the average metallicity for terrestrial planets ( $R_p < 1.7R_{\oplus}$ ) is consistent with the solar metallicity at  $\sim 0.02 \pm 0.02$  dex. With their larger sample, it was clear that stars with either gas-giant planets or gas-dwarf planets were preferentially metal-rich, suggesting a planet-metallicity correlation for these two types of planets. However, it remains unclear whether such correlation exists for rocky planets. Wang and Fischer (2013) examined the same dataset as Buchhave *et al.* (2014). After accounting for systematic errors of stellar properties from the Kepler Input Catalog, Brown *et al.* (2011), they reported a modest planet-metallicity correlation for terrestrial planets at  $4.2\sigma$  level.

Many stars in the solar neighborhood are components of multiple-star systems (Duquennoy and Mayor, 1991; Fischer and Marcy, 1992; Raghavan *et al.*, 2010; Duchêne and Kraus, 2013) and many planets have been detected in binary or multi-star systems. Initially, exoplanets were discovered orbiting one individual

star in the binary star system (Cochran *et al.*, 1997; Eggenberger *et al.*, 2004). Recently, exoplanets have been discovered in difficult to detect circumbinary orbits, where the planet orbits both stars (Doyle *et al.*, 2011; Welsh *et al.*, 2012; Schwamb *et al.*, 2013).

Circumbinary planets can be detected via the timing variation of eclipsing binaries (Deeg *et al.*, 2008; Beuermann *et al.*, 2010). Since the launch of the *Kepler* mission, ten circumbinary exoplanets have been discovered around eight *Kepler* stars. The occurrence rate of circumbinary planets is estimated to be  $\sim 10\%$  (Welsh *et al.*, 2014; Armstrong *et al.*, 2014) assuming the orbital plane of circumbinary planets roughly align with the binary orbital plane. The occurrence rate could be much higher if the orientation of planet orbits is more isotropic.

It is expected that planet formation may be impeded in systems where the binary stars have small separations (e.g.,  $\sim 10\text{--}200$  AU). This is supported both by simulations (Th ebault *et al.*, 2006; Kley and Nelson, 2008; Thebault, 2011) and observations (Desidera and Barbieri, 2007; Kraus *et al.*, 2012; Wang *et al.*, 2014) that find a smaller fraction of exoplanets in binary star systems. It is not surprising that the dynamics of binary star systems stir things up and challenge planet formation. What is surprising is that the planets exist there at all.

Our view of exoplanets is still skewed by the observational sensitivities of the techniques that we use. However, the discoveries that have been made have helped us to revise our understanding of planet formation and the formation of the solar system. We see that planet formation is a chaotic process and that disks are sculpted by gravitational interactions to a greater extent than we appreciated by considering our own solar system. We now know that almost every star has planets and that planet formation is far more robust than astronomers expected.